

INBOUND WAVES IN THE SOLAR CORONA: A DIRECT INDICATOR OF ALFVÉN SURFACE LOCATION

C.E. DEFOREST¹, T.A. HOWARD¹, AND D.J. MCCOMAS^{2,3}

¹Southwest Research Institute, 1050 Walnut Street, Boulder, CO, USA

²Southwest Research Institute, 6220 Culebra Road, San Antonio, TX, USA and

³University of Texas at San Antonio, TX

Author preprint: accepted for Astrophysical Journal, 11-April-2014

Abstract

The tenuous supersonic solar wind that streams from the top of the corona passes through a natural boundary – the Alfvén surface – that marks the causal disconnection of individual packets of plasma and magnetic flux from the Sun itself. The Alfvén surface is the locus where the radial motion of the accelerating solar wind passes the radial Alfvén speed, and therefore any displacement of material cannot carry information back down into the corona. It is thus the natural outer boundary of the solar corona, and the inner boundary of interplanetary space. Using a new and unique motion analysis to separate inbound and outbound motions in synoptic visible-light image sequences from the COR2 coronagraph on board the *STEREO-A* spacecraft, we have identified inbound wave motion in the outer corona beyond $6 R_s$ for the first time, and used it to determine that the Alfvén surface is at least 12 solar radii from the Sun over the polar coronal holes and 15 solar radii in the streamer belt, well beyond the distance planned for NASA’s upcoming Solar Probe Plus mission. To our knowledge this is the first measurement of inbound waves in the outer solar corona, and the first direct measurement of lower bounds for the Alfvén surface.

Subject headings: Sun: corona, Sun: fundamental parameters, Sun: solar wind, techniques: image processing

1. INTRODUCTION

The solar corona is distinguished from the solar wind by dynamical means. Coronal plasma is, on average, continuously expanding into interplanetary space to form a fast wind (Parker 1958; Neugebauer & Snyder 1962) that forms the heliosphere (Parker 1961; Axford et al. 1963). In the corona, the plasma motion is slower than the speed of the MHD wave modes. In the heliosphere, the plasma is super-Alfvénic, so that information cannot propagate inward and affect the morphology or connectivity of the solar corona. The two regions are divided by a boundary, the “Alfvén surface”, at which the wind speed exceeds the Alfvén speed (formally the fast magnetosonic speed, but we use the term “Alfvén speed” throughout this study as they are equal in the field-aligned direction and the local magnetic field is nearly

radial in the outer corona). This boundary has also been called by several other names, among them the “heliobase” (Zhao & Hoeksema 2010), the “Alfvén point” (Hundhausen 1972), and the “Alfvén radius” (Goelzer, et al. 2014).

The Alfvén surface is fundamental to the magnetic topology of the solar corona and heliosphere. Magnetic flux that passes through Alfvén surface boundary is referred to as “open” in the context of coronal physics. Because usage of “open” has diverged and become ambiguous across both the solar remote sensing and heliospheric in-situ sensing communities, we use the phrase “Alfvén open” to distinguish field lines that cross through the Alfvén surface, from field lines that pass through other important surfaces or qualify as “open” under other definitions.

In addition to its importance for the corona and for MHD simulations, the Alfvén surface

should be detectable remotely via motions in the visible corona. Outside the Alfvén surface, all collective motions of the plasma must propagate outward from the Sun. Inside the Alfvén surface, such motions may propagate both outward and inward. Verdini, Velli & Buchlin (2009) modeled the speed-vs-radius behavior of inbound waves, which yield a specific signature of slow inbound propagation near the Alfvén surface. It should be possible to identify the approximate location of the Alfvén surface in different regions of the corona by examining the spatial spectrum and relative intensity of inward and outward propagating disturbances in images of the outer corona, provided that sufficiently low-noise measurements are available and an analysis technique can be developed to separate the upward and downward motions. This latter requirement comes from the fact that, except in special circumstances such as the retracting of *inner* coronal loops below $6 R_s$ (McKenzie & Hudson 1999; Wang et al. 1999; Sheeley et al. 2001; DeForest, Howard & McComas 2012), the outward motion is so dominant that it is extremely difficult to discern any inward motion at all.

Consideration of the Alfvén surface to date has been mostly theoretical (that is, it has been considered primarily using theory, models and simulations), with treatments dating back to the division of ideas regarding the expansion of the corona between Chapman (1957) and Parker (1958) in the 1950s. Parker (1958) first suggested that there was a division between the corona and the solar wind, while Hundhausen (1972), in a review summarizing the theoretical developments of the expanding corona leading to the early 1970s, described the nature of this division in terms of the transition from “closed” to “open” magnetic field lines. Several recent works suggest a broad range of possible distances for the Alfvén surface, from 10–30 R_S . Zhao & Hoeksema (2010) used observations of helmet streamers in the corona to model the Alfvén surface, placing its outer limit at 10–14 solar radii (R_S) around solar minimum. Wang et al. (1999), and Sheeley & Wang (2001), and Sheeley et al. (2004) have observed isolated inbound retracting loops in streamers; never observing such a feature beyond $6R_s$, they attribute this lack to a low Alfvén surface near $6R_s$. Schwadron et al. (2010) and Smith, et al.

(2013) treat the Alfvén surface in the context of the heliospheric flux balance, and place it at 10–15 R_S . Goelzer, et al. (2014) have applied a simple model of the heliospheric magnetic field to in-situ measurements of the solar wind and place the surface around 15 R_S at solar minimum and 30 R_S at solar maximum.

In the present work, we report on the first detection and measurement of inbound wave and other motions in the outer corona, using synoptic data from *STEREO/COR2* (R. Howard et al. 2008) and post-processing to separate image features by characteristic direction of motion. We have measured signatures of inbound motion, which we attribute to propagation of compressive waves in the corona (e.g. DeForest & Gurman 1998), over the full range of altitudes viewed by COR2 in the streamer belt, and out to 12.5 R_S in the polar coronal holes. Based on these measurements, we conclude that the Alfvén surface is typically above $15R_S$ in the streamer belt and well above 12 R_S in the polar coronal holes in solar minimum conditions. In Section 2 we describe the theory of measurement; in Section 3 we describe the dataset we analyzed and the techniques used to prepare inbound and outbound images; in Section 4 we present direct results of the analysis; and in Section 5 we discuss their implications and required follow-on analysis, before summarizing the work in Section 6.

2. THEORY OF MEASUREMENT

To understand the expected visual signature of waves in the outer corona, we briefly discuss the theory of coronagraphic measurement. Coronagraphs record Thomson-scattered light from the optically thin corona. The viewing angles are small and it is customary to approximate viewing coordinates with a Sun-centered Cartesian coordinate system (x, y, s) , where the first two coordinates are scaled from the image plane and the third is distance along each line of sight. The local differential radiance of the corona depends on the local electron density and a geometric function that varies only slowly with s (e.g. Billings 1966). Other sources of pixel brightness include the starfield, F corona, and instrument stray light (e.g. Lyot 1939; Brueckner et al. 1995). Through post-processing one typically eliminates (or at least greatly reduces) these background sources, so

that the processed coronal radiance B' is given by:

$$B'(x, y, t) \approx k(r) \int ds (n'_e(x, y, s, t)) + N'(x, y, t) \quad (1)$$

where r is focal-plane radius from the Sun; k is a per-radius constant of proportionality that includes the instrument calibration geometric factors, mean solar radiance, and Thomson scattering physics; N' is a residual noise term, which includes photon statistics and also unsubtracted background; and $n'_e \equiv n_e(x, y, s, t) - n_0(x, y, s)$ for some baseline time-independent n_0 that is subtracted as part of the estimation and removal of the background sources (e.g. Morrill et al. 2006). Because of the steep radial gradient in density within the corona, the integral in Equation 1 is dominated by the region where $s \ll r$, i.e. the “sky plane” (e.g. Fisher & Guhathakurta 1995).

A “feature” or bright patch in B' generally represents a locus of enhanced density in the solar corona (an “object” or “structure”), and a moving feature (i.e. one that exhibits displacement in subsequent images) thus represents either true motion of dense coronal material, propagation of a compressional wave signal through the coronal medium, or some combination of these. An additional possible source of apparent motion is alignment between the line of sight and an extended structure such as a slightly curved thread or sheet in the corona; these “caustic effects” can in principle cause rapid apparent motion as a result of slight changes in the position or shape of the structure. These effects only occur during rare coincidences and we presume them to be negligible.

Pure Alfvén waves themselves include no variation of density and hence are not visible with a coronagraph; but fast-mode MHD waves are visible and propagate at speeds between V_A and $V_{Fmax} = \sqrt{C_s^2 + V_A^2} \approx V_A$ relative to the medium, where C_s is the speed of sound, V_A is the Alfvén speed, and C_s/V_A is the plasma β parameter, which is generally small in the corona (e.g. Priest 1982). Above the lowest layers of the corona, outward wind flow dominates the plasma motion (e.g. Parker 1958; Hundhausen 1972), so that measured inbound motion of features in B' is most frequently caused by wave action, although retraction of loops,

with corresponding plasma motion, is seen in and around the streamer belts at altitudes below $6R_s$ (e.g. Wang et al. 1999; Sheeley & Wang 2001; Sheeley et al. 2004). Note that, although wave fields are commonly described using the plane wave basis, wave motion is not required to have any oscillatory character at all. Wave-related motion or density enhancement can have a smooth, pulse, complex, or oscillatory character depending on the excitation and any resonances in the system supporting the waves. In the corona, we expect to observe waves that are excited by the passage of outbound coronal structures such as coronal mass ejections, blobs (Sheeley et al. 2009), or disconnected U-loops (McComas et al. 1991; DeForest, Howard & McComas 2012). These waves are needed to carry the inbound signals that describe and set the new equilibrium shape of the corona.

Waves propagating in a moving medium are advected with the medium, so that if the bulk radial wind speed $V_{w,r}$ be significantly greater than the Alfvén speed V_A , no inbound features should be observed at all. But if the bulk radial wind speed $V_{w,r}$ happens to be significantly less than the Alfvén speed, then inbound features should be detected - particularly after passage of a CME, blob, or other localized disturbance that causes a shift in the coronal equilibrium. Such shifts can only propagate inward at speeds up to $V_A - V_{w,r}$, and should be visible in carefully prepared image sequences, just as they are in modeled image sequences of the wind acceleration region (e.g. Verdini, Velli & Buchlin 2009).

In practice, such features have never (to our knowledge) been observed beyond a few R_S in the coronal holes, though inbound wave signals must be present if (as is observed) the inner corona reacts to large scale changes above altitudes of $4 - 5 R_S$. One reason for this lack may be that the unaided eye has difficulty separating the presumably-faint inbound wave signal from a far greater optical flow¹ of outbound features. We overcame this difficulty by using

¹ Readers are reminded that “optical flow” is the pattern of apparent motion in a visual scene, as distinct from actual flow of structures imaged in the scene. We use the phrase to refer to the image energy that is present within a particular range of velocities, as distinct from the apparent-to-the-eye motion of individual features in the scene.

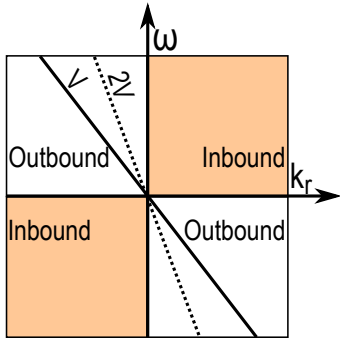


Figure 1. Fourier transformation localizes moving features by speed and direction. Features moving with speed V in the (r, t) plane are transformed to features lying along the indicated line in the (k_r, ω) plane, which is segmented into inbound and outbound quadrants as marked. Doubling the speed to $2V$ doubles the slope of the line.

Fourier transformation to separate fully the inbound and outbound features in the coronagraphic image data.

Converting B' from Cartesian (x, y, t) to polar (θ, r, t) coordinates yields a movie in which radial motion is purely vertical. Fourier transformation from r and t to wavenumber k_r and frequency ω localizes all moving features in the movie, regardless of size or location, to the line through the origin whose slope is equal to the radial speed of the feature (see the Appendix). Figure 1 shows the location of inbound and outbound image features in the (k_r, ω) plane (neglecting the sky-plane azimuthal angle θ or its inverse, k_θ). By masking out unwanted parts of the (k_r, ω) Fourier plane and then analyzing the remaining energy in the images, we were able to search for inbound features, in the absence of distraction from the dominant outward motion.

Two kinds of non-directional signals are captured by the Fourier quadrant filter shown in Figure 1. First, non-moving features such as the streamer belt itself are formed of equal parts inbound and outbound energy in Fourier space, and therefore they appear in both inbound and outbound sequences. Fortunately, the only non-moving features in the corona are also quasi-stationary, i.e. they exist at low ω only. These features can be removed by simply zeroing the low- ω portion of the dataset, an operation that is similar to unsharp masking in time. Secondly, isotropic noise sources such

as the photon noise contain an isotropic mix of wave signals and therefore appear equally in the inbound and outbound portions of the separated movie. These noise sources are identifiable precisely because they are nearly isotropic: they can be eliminated by searching for structure in the filtered data, such as a narrow range of speeds far from any characteristic speed of the filters that have been applied. Wave signals in the data are expected to propagate at the local wave speed corrected for advection, while the only characteristic speeds in the noise should be any that are imposed by the filtering and data-preparation process.

3. DATA & METHODS

We sought to identify the Alfvén surface in a sequence of coronagraph images from *STEREO-A/COR2* (R. Howard et al. 2008) by searching for inbound feature motion through a sequence of coronagraph images. We selected 2007 August 4–14 as a quiet period near solar minimum with a small amount of coronal activity and no instrumental anomalies. We downloaded the Level 0 data from the *STEREO* web site, processed it to Level 1 with the *SECCHI PREP* program available via Solarsoft (Freeland & Handy 1998), and carried out several further nonstandard steps to improve and regularize the data. First, we prepared a model F corona by smoothing each Level 1 image by a 9-pixel-diameter tophat kernel,² then taking the 1 percentile value (i.e. 5th lowest) of the 512 values for each pixel in the data set. We subtracted this model F corona from each frame to produce a K coronal movie; these are the “L1-F” data, and a typical frame is shown in the left panel of Figure 2.

Because we sought to find wavelike patterns in the data, we needed to minimize the residual starfield (frequently ignored in coronagraph analysis). We applied the *spikejones* despiking algorithm (DeForest 2004a) to each frame of the L1-F data. This was sufficient to remove most visible stars but left wide PSF-derived

² Readers are reminded that a “tophat kernel” is a generalization to two dimensions of the familiar “boxcar kernel” in one dimension. It is constructed by starting with an image containing all zeroes, then setting all pixels within a given radius of the center to unity and all pixels outside that radius to zero. Finally, the kernel is normalized to a sum of unity.

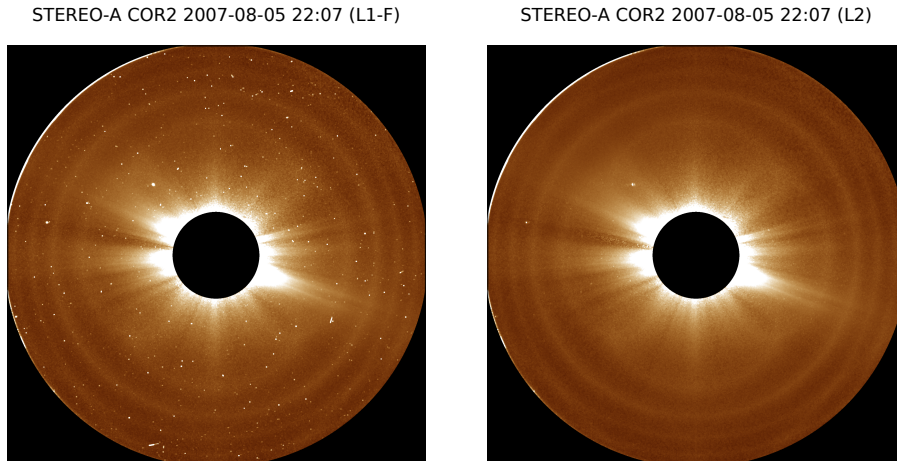


Figure 2. We prepared COR2 data by generating (and subtracting) an *ad hoc* F coronal model (left), and then further despiking the data (right) to remove most stars.

“halos” from most bright stars. To further reduce the effect of the starfield, we considered each pixel in the dataset as a time series. We generated a smoothed copy of the time series by applying a 9-frame median filter, and identified the values in the original data whose difference from this median-smoothed copy was the greatest. We set the corresponding pixel in each of the the 10 frames with the highest difference value, to the timeseries median. This had the effect of removing most data dropouts and most stellar halo effects from the image sequence. We called these data Level 2, and a typical frame is shown in the right panel of Figure 2.

The additional postprocessing with *spikejones* and the median filter eliminated most stars, but small “halos” are still present around the very brightest objects (such as the planet Mercury and the brightest few stars). These remain faintly visible in the data and are highlighted by the subsequent processing steps, but are clearly identifiable from their slow motion and compact form.

To give better access to radial motion of differential signals, without regard to the over-

all gradient in radiance, we resampled each image into radial coordinates, and normalized with a radial filter. The resampling step used a spatially-variable resampling filter to avoid introducing moiré artifacts (DeForest 2004b). We normalized radially by subtracting from each row its mean value across column and time, then dividing the row by its variance (RMS value) across column and time. The result is a radial-coordinate frame such as Figure 3. We transposed the sequence of radial frames into a collection of (radius, time) evolution images, one at each of 720 azimuthal angles.

To isolate moving signals, we Fourier transformed the radialized image sequence in radius and time, and divided the (k_r, ω) plane into quadrants to separate the data into inbound and outbound sequences. At this stage, we also imposed a motion filter, rejecting all features moving slower than 1 pixel per frame (19 km sec^{-1}) and all features moving faster than 47 pixels per frame (900 km sec^{-1}). These speeds were selected to be broad enough to capture features moving between a significant fraction of the sound speed and the Alfvén speed, but do not themselves hold any particular signifi-

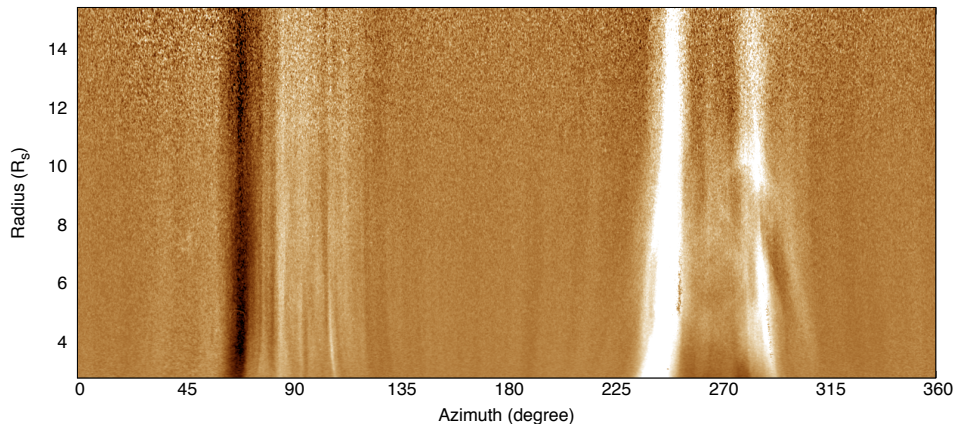


Figure 3. Radialized COR2 frame shows prepared, radialized images prior to motion filtering.

cance. The motion filtering removed the stationary and quasi-stationary streamer signals, making a motion signal easier to perceive. The theory of motion-filtering and our application of it are described in more detail in the Appendix.

Also we smoothed each radialized frame by convolution with a 5 pixel full-width Gaussian in the image plane (i.e. an elliptical Gaussian with 2.5 degrees full-width in azimuth and $0.2 R_s$ in radius). This further reduced image noise, especially in the outer portions of the image plane where the original signal is faint. One of these fully filtered frames is pictured in Figure 4, divided into inbound and outbound images. The full set of filtered frames is available as a supplementary movie in the digital version of this article; the respective outward and inward motions are clearly apparent in the movie.

The fully filtered data form a pair of data cubes with independent variables of azimuth, radius, and time. Figure 4 is a constant-time slice of the two data cubes, at 2007 August 8 21:37 UT. It is more instructive to view a particular azimuth slice, plotting filtered radiance against time and radius. Figure 5 is such a slice, averaged over 2° of azimuth. The averaging further beats down noise in the original data, and was chosen to match the observed 2° size of coronal features such as polar plumes (e.g. Fisher & Guhathakurta 1995). Again, the full dataset is available in the digital version of

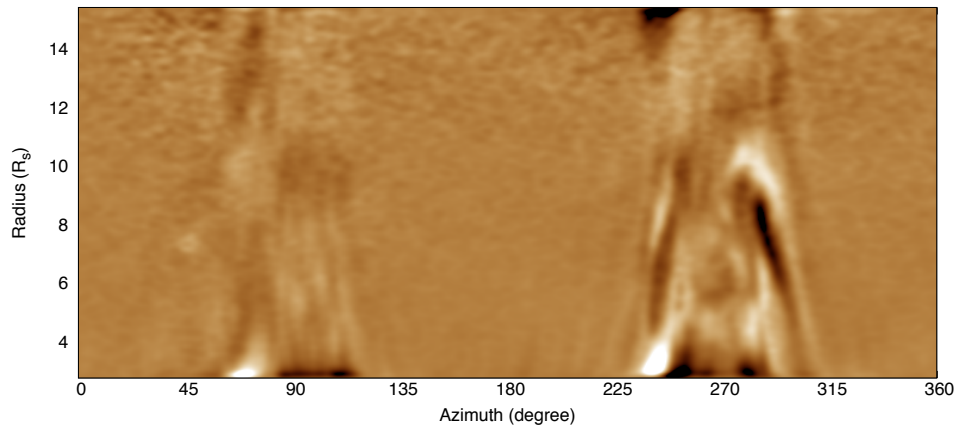
this article, as a movie that runs over azimuth. Viewing the data in this way reveals azimuthal structure in the corona.

4. RESULTS

Both Figure 5 and Figure 6 show evidence of inbound features in the solar corona. Each figure has outbound features in the top panel and inbound features in the bottom panel. Each panel's brightness scale is set to ± 2.5 times the calculated variance of the filtered radiance, and the mean value has been subtracted from the image. Because of the radial normalization, the motion-filtered radiance is in units of the measured pixel-value variance at each radius from the Sun. For example, a value of $+0.1$ indicates a feature that is brighter than the mean radiance at its radius from the Sun, by 10% of the RMS variation of the original pre-filtration data at that radius; and a pixel value of -0.01 indicates a feature that is fainter than the mean by 1% of that RMS variation.

Because of the complexity of the dynamics of the streamer belt, and the relative simplicity and faintness of the coronal hole, we analyze and report results from those two portions separately. In the streamer belt there are sufficient visually distinguishable features to demonstrate inbound wave motion from particular excitation events; in the coronal hole, it is both necessary and possible to perform speed-spectrum analysis of the optical flow in the scene.

COR-2A: 2007 Aug 08 21:37 OUTBOUND FEATURES



COR-2A: 2007 Aug 08 21:37 INBOUND FEATURES

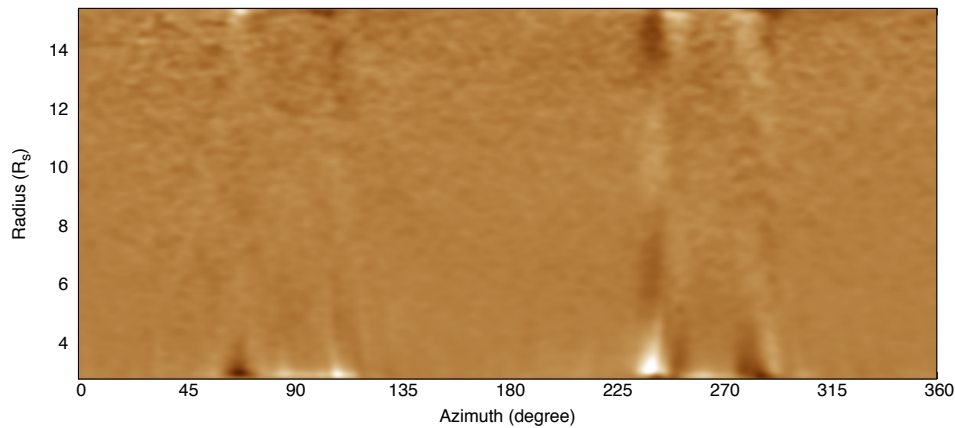


Figure 4. Fully filtered and inbound/outbound separated COR2 frame shows lower noise and lack of stationary streamer compared to Figure 3. TOP: outbound features show a CME in progress over the east limb (270°). BOTTOM: inbound features show ringing near the edges of the streamers, and a weak return signal. The full movie is available as a supplement in the digital version of this article.

4.1. Streamer Belt

Figure 5 has several important outbound features. Two CMEs erupted from the eastern streamer during this observation, and are visible in the movies that accompany the online edition. The first, at about 60 hours from the start of the data set, was a small CME traveling at $280 \pm 20 \text{ km s}^{-1}$ between 8 and $14 R_S$, based on direct measurement of the feature's slope in the plotted image. The second, at about 110 hours from the start of the data set, was a larger CME traveling at a slower speed of $170 \pm 15 \text{ km s}^{-1}$ across that height range. Throughout the

sequence, small outbound features may be seen propagating at speeds from $150\text{--}400 \text{ km s}^{-1}$; these appear to be the familiar “blobs” analyzed by Sheeley et al. (2009).

Inbound features in Figure 5 include several residual star tracks, annotated in the figure; myriad diffuse inbound features in the lower corona, four of which are circled between 150–250 hours; and returning inbound features from the first CME. Two clear inbound features may be seen. First, a small, compact, bright inbound feature may be a fast mode wave or retracting loop. The two are both expected to

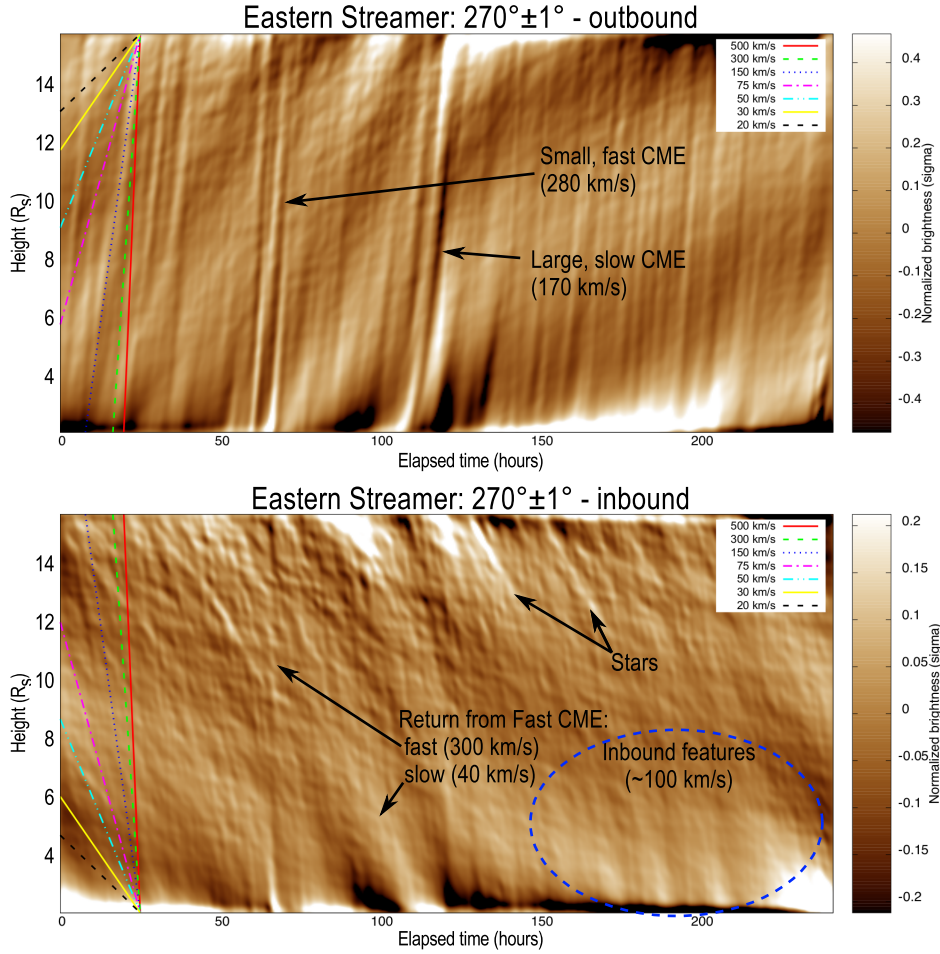


Figure 5. Time/radius diagrams of filtered, separated COR2 data at azimuth= 270° show inbound and outbound features in the streamer belt, including stars, CMEs, and an inbound CME return signal. Speed is represented as slope in these images. Several fiducial speeds are plotted as overlain lines.

propagate at the fast speed $V_f \sim V_A$, and the observed feature speed is $\sim 300 \text{ km s}^{-1}$. The second is a more diffuse, bright inbound feature moving at $\sim 40 \text{ km s}^{-1}$, which is consistent with a slow speed $V_s \sim C_s \sim 100 \text{ km s}^{-1}$, slowed by outbound bulk motion of order 50 km s^{-1} . Both return signatures intersect the outbound CME in the range $12\text{--}14 R_S$.

Several other bright, easily distinguished inbound features are present and annotated in Figure 5, propagating at speeds between $40\text{--}100 \text{ km s}^{-1}$, and the compact, bright, slower-moving star tracks in the outer portion of the image. Because these features are easily recog-

nized by eye, and are present with essentially constant inbound speed at altitudes as high as $12\text{--}13 R_S$, we immediately conclude that the Alfvén surface is at least that high; this result is refined in Section 5.

Superposed on the large-scale pattern is a lower-amplitude, more complex background signal that is present at all azimuths. Because this background signal is present both in the streamer belts and in the coronal holes, where it is not mixed with the larger-scale evolution of the CMEs and blobs, we analyze it primarily in the coronal holes.

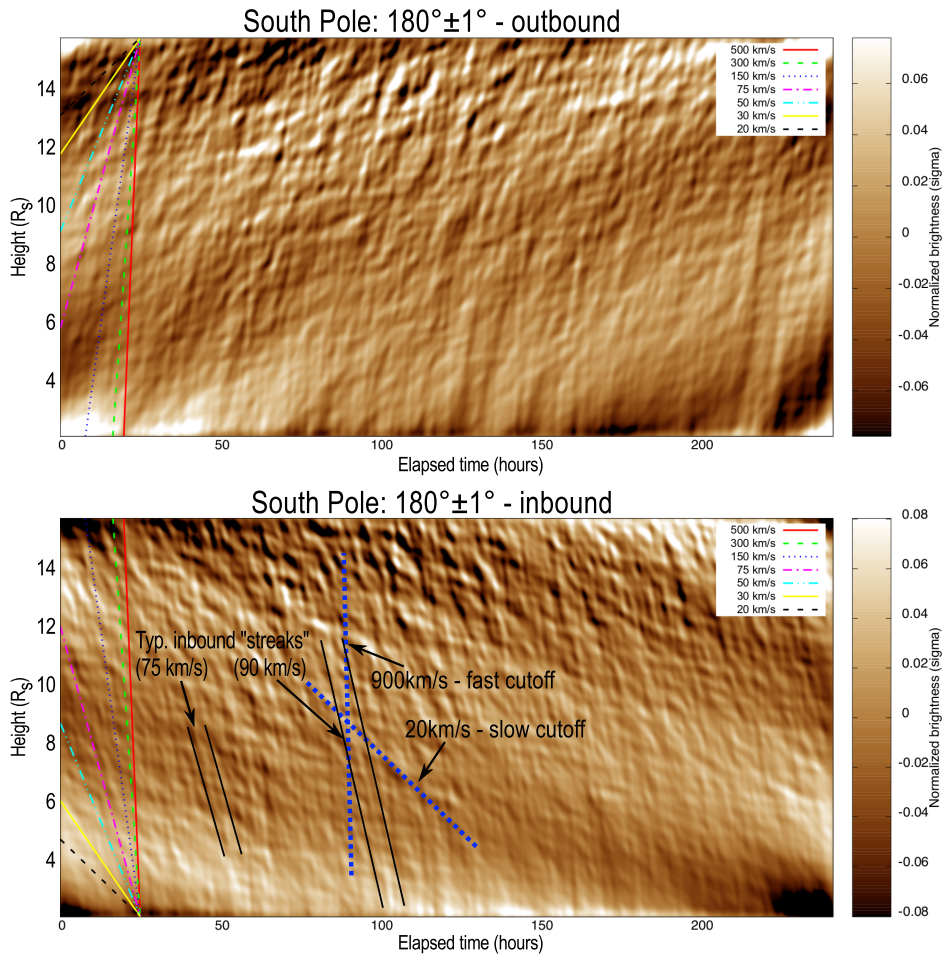


Figure 6. Time/radius diagrams at azimuth= 180° show inbound and outbound features over the polar coronal hole. The inbound features are distinguishable from noise by their well-defined characteristic speed, far from the cutoff speeds of the motion filter.

4.2. Coronal Hole

Figure 6, being from the center of the southern polar coronal hole, lacks the large-scale structures evident in the streamer belt. It is thus simpler and easier to distinguish the background signal, which has a complex character that at first glance is difficult to distinguish visually from noise. There is a strong characteristic speed to the background, as evidenced by the long, narrow appearance of individual fluctuations. These have a characteristic inbound speed of $40\text{--}90\text{ km s}^{-1}$, varying across the data set, which may be read directly from the typical slope of the long, narrow fluctua-

tions. The lower speed bound of $\sim 40\text{ km s}^{-1}$ is $\sim 2\times$ faster than the slow cutoff speed of the processing, indicating it is not an artifact of the motion filter. The corresponding characteristic outbound speed of the fluctuations in the outbound panel is $200\text{--}400\text{ km s}^{-1}$. These speeds are consistent with an outbound subsonic wind with fast-mode Mach number in the range $0.5\text{--}0.8$ assuming that the average between the typical inbound and outbound velocities represents the bulk speed and the difference represents twice the wave speed.

The structure of the inbound features, in particular, is important for distinguishing them

from noise. Typical long, narrow features may be traced through 4-5 R_S of inbound motion compared to their instantaneous radial sizes of under 0.5 R_S . Typical features span over 10 hours of elapsed time. This degree of elongation distinguishes them from noise. Noise features may be expected to be incoherent on timescales comparable to the instantaneous size of the feature, divided by the difference between the two cutoff speeds of the motion filter – i.e. 1-2 hours for features similar to the annotated one. The characteristic speeds of the motion filter are shown in Figure 6 to illustrate that the fluctuations’ typical speeds are both well defined and well between the filter cutoff speeds. In particular, incoherent noise filtered through our motion filter would produce “bowtie” features with similar opening angle to the two filter speeds. The observed fluctuations are more coherent.

To better characterize the speed of the inbound features and to demonstrate that they are not noise, we prepared a speed spectrum vs. altitude over the south pole of the Sun. We prepared this spectrum by selecting a $50 \text{ h} \times 1.2 R_S$ region of Figure 6 and convolving it with a diagonal line at a particular speed, then calculating the RMS value of the convolved image. This RMS value formed a single pixel of a (speed, radius) planar image, and we iterated over both speed and central radius from the Sun of the extracted patch. After generating all the RMS values, we normalized each row (i.e. constant-radius locus) in the image to set its maximum value to unity. We repeated the entire process for 5 randomly chosen 50 h intervals, and collated a single image out of the median value of each pixel over those 5 intervals. The result is the speed spectrum shown in Figure 7. The inbound features form a well-defined, if slightly broadened, ridge relating speed and distance from the Sun. The coherence of the ridge indicates the presence of well-formed inbound movement at all radii out to 12 R_S . Above 12 R_S a clear ridge is not present, which likely indicates that the noise floor dominates the measurement above that altitude. Below 7 R_S , no clear ridge is visible – but this is not surprising, because the extrapolated speed of the ridge would be below the motion-filter cutoff speed imposed during preprocessing.

Because of the well-defined speed spectrum

ridge, we identify the polar inbound features as inbound waves. We would not expect clear structure in the accidental speed profile of an ensemble of individual packets of plasma that had been accelerated by different events; but such structure is in fact expected for waves, whose speed is controlled by the mostly-uniform medium that supports them. We identify the characteristic speed as the upstream wave speed $V_A - V_{wind}$, and note that the generally increasing trend in inbound speed with altitude indicates that the wave speed was increasing faster with altitude than was the wind speed.

As a check on our interpretation of the speed data, we compare the ridge speeds from Figure 7 to rough estimates of the wind and Alfvén speed. Taking the average Alfvén-open flux density to be $\sim 10 \text{ G}$ at the photosphere (DeForest et al. 1997), and the linear expansion factor to be ~ 2 (DeForest et al. 2001), the average magnetic field strength at 10 R_S is 20 mG. Taking the typical coronal hole electron density at 10 R_S to be $n_e = 2 \times 10^4 \text{ cm}^{-3}$ (DeForest, et al. 2001) yields an Alfvén speed $V_A \approx 300 \text{ km s}^{-1}$. Typical modeled solar wind speeds at this altitude are in the range of $V_w \approx 200\text{-}300 \text{ km s}^{-1}$ (e.g. Cranmer et al. 2013), which is consistent with the interpretation that the ridge is formed by waves moving at the upstream speed $V_A - V_w$.

5. DISCUSSION

The primary physical difference between the solar corona and the solar wind is the presence of inward-propagating wave signals. By separating coronal features by inbound vs. outbound optical flow direction, we have demonstrated, for the first time, remote measurement of these inbound waves in the outer solar corona above 5 R_S . Based on the observed properties of inbound features, we have determined a lower limit for the Alfvén surface altitude of 15 R_S in the streamer belt and 12 R_S in the coronal hole. The height of the lower bound is set in the streamer belt by the field of view of the instrument, and in the coronal hole by the noise properties of the particular data set we used.

There is evidence that the polar Alfvén surface is much higher than 12 R_S . The propagation speed of the inbound waves appears to

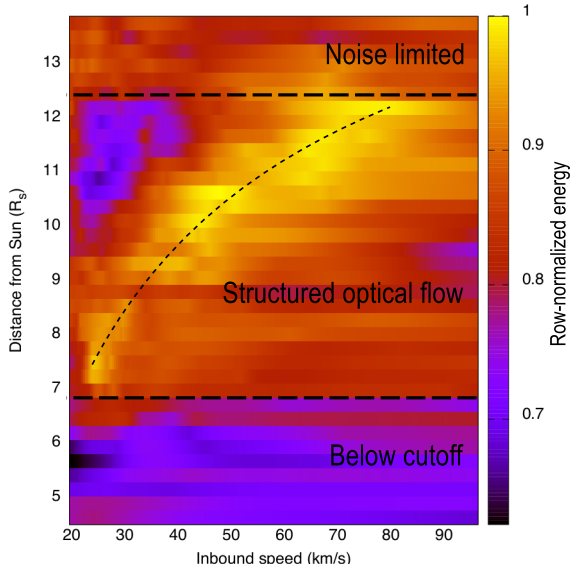


Figure 7. Inbound speed spectrum vs. altitude in the polar region shown in Figure 6 reveals structure in the seemingly random fluctuations of inbound coronal radiance. The fluctuations have a well-defined characteristic speed that varies with height; we take this as evidence that the fluctuations are inbound waves, propagating with the upstream wave speed $V_A - V_w$; and that the Alfvén surface is well above the $12 R_S$ noise limit of the present observation.

increase with height, which is the opposite direction of variation from our *a priori* expectations. Near the Alfvén surface, the inbound wave speed must drop to zero with increasing altitude, and the fact that the ridge in Figure 7 is still increasing in speed as it reaches the noise floor at $12 R_S$ implies a further significant height range in which the inbound speed decreases smoothly to zero. We surmise that a smooth transition to zero would require at least a few R_S , and therefore that the Alfvén surface must be at least several R_S above the top of the observed ridge in Figure 7. Deeper coronal exposures, and/or a wider field of view, are necessary to extend the measurement further from the Sun. It is neither necessary nor expected that the Alfvén surface will prove to be spherical, smooth, or time-invariant.

As with all purely image-based measurements of motion, the data themselves cannot directly distinguish between bulk motion and wave motion. In our streamer belt analysis, this ambiguity is particularly keen in the case

of the downward signature of the first CME in Figure 5. Fortunately for the present study, both bulk retraction of a loop and a downward propagating density wave are limited by the fast-mode speed of the medium: we are able to use the retraction to place a lower limit for the Alfvén surface location, regardless of whether it be a tension-force-driven bulk motion or a pure inbound wave. The inbound fluctuations observed in the coronal hole are wholly new and identification is important to understand the phenomenon being observed. The coherence of individual fluctuations in Figure 6 indicates that the features are not noise. The observed smoothly-varying preferred speed versus radius strongly indicates wave motion, because individual features would be expected to have a broader range of speeds and no coherent ridge structure. The ridge pattern indicates that the motions are governed by bulk properties of the corona rather than by the accidental circumstances of formation of myriad small dense objects, and the obvious bulk properties are the general outflow speed and MHD wave speeds.

The Alfvén surface is important both as a boundary of the corona and because of its important topological properties with regard to the magnetic field. Magnetic field lines that exist entirely inside the Alfvén surface are “Alfvén closed” and can move up or down through the corona, or even in principle disappear entirely if their footprints in the photosphere merge in the process of cancellation, which is associated with submergence of magnetic flux under the photosphere (e.g. Schrijver et al. 1997; DeForest et al. 2007). Field lines that penetrate the Alfvén surface are “Alfvén open” in the sense that they cannot retract into the Sun. A coronal loop, CME, or connected bolus of ejecta that travels beyond the Alfvén surface must necessarily increase the heliospheric magnetic flux, because the particular field lines now connect the Sun to the heliosphere. Because it is impossible to retract these Alfvén-open field lines, balancing the insertion of new magnetic flux through the Alfvén surface into the heliosphere requires disconnection of Alfvén-open field lines and subsequent ejection of U-shaped loops outward through the Alfvén surface (McComas et al. 1992; McComas 1995; Schwadron et al. 2010). Reconnection above the Alfvén surface cannot affect the coronal flux balance

or morphology; reconnection below the Alfvén surface is necessary to prevent the interplanetary magnetic field from growing without limit.

Detecting and measuring the wave field in the outer corona is an important step toward using the wave field as an independent measure of solar wind acceleration and other coronal properties throughout the outer corona. With better noise levels, it should be possible to map the Alfvén surface directly. Even more importantly, it should be possible, with improved noise levels and a custom observing campaign, to measure the wind speed and outbound wave speed directly in the coronal hole. Measuring all three, and incorporating photometric measurements of the coronal density, will enable independent determination of V_A and the magnetic field B across height throughout the important acceleration region of the solar wind.

6. CONCLUSIONS

We have, for the first time, detected inbound compressive waves in the outer solar corona, and used them to set a strong lower limit on the location of the Alfvén surface that marks the top of the solar corona and beginning of the solar wind. We accomplished this measurement by separating inbound and outbound density features through a Fourier transform analysis of existing synoptic coronagraph data. We find that the Alfvén surface was above $15 R_S$ in the streamer belt and significantly above $12 R_S$ in the polar coronal holes. These limits imply that the upcoming Solar Probe Plus mission planned by NASA to plunge repeatedly within $10 R_S$ should routinely observe the subsonic solar wind and corona in-situ. These limits are set by the field of view of the instrument, and the noise characteristics of this particular measurement, respectively. This initial detection and measurement of the inbound wave field is an important first step toward direct measurement of plasma properties throughout the entire solar wind acceleration region.

This work was supported under grant from NASA’s Heliophysics SHP-SR program. D. Mc. was supported via the SWEPAM instrument on NASA’s ACE mission. The authors gratefully acknowledge the STEREO team for making their data available to the public, and Marco Velli for illuminating and helpful discus-

sion. The analysis relied heavily on the free-ware Perl Data Language (<http://pdl.perl.org>).

REFERENCES

- Axford, W.I., Dessler, A.J., and Gottlieb, B. 1963: *Astrophys. J.* 137, 1268.
- Billings, D.E. 1966: “A Guide to the Solar Corona”, Academic Press (New York).
- Bracewell, R. 1999: *The Fourier Transform and Its Applications*, 3rd Edition, McGraw-Hill (New York).
- Brueckner, G.E. et al. 1995: *Sol. Phys.* 162, 357.
- Chapman, S. 1957: *Smithsonian Contrib. Astrophys.* 2, 1.
- Cranmer, S.R., van Ballegoijen, A.A., and Woolsey, L.N. 2013: *Astrophys. J.* 767, 125.
- DeForest, C.E. et al. 1997: *Sol. Phys.* 175, 393.
- DeForest, C.E. and Gurman, J.B. 1998: *Astrophys. J.* 501, L217.
- DeForest, C.E., Lampy, P.L., and Llebaria, A. 2001: *Astrophys. J.* 560, 490.
- DeForest, C.E., Plunkett, S.P., and Andrews, M.D. 2001: *Astrophys. J.* 546, 569.
- DeForest, C.E. 2004a: *Astrophys. J.* 617, L89.
- DeForest, C.E. 2004b: *Sol. Phys.* 219, 3.
- DeForest, C.E., Hagenaar, H.J., Lamb, D.A., Parnell, C.E., and Welsch, B.T. 2007: *Astrophys. J.* 666, 576.
- DeForest, C.E., Howard, T.A., and Tappin, J. 2011: *Astrophys. J.* 738, 103.
- DeForest, C.E., Howard, T.A., and Mcomas, D.J. 2012: *Astrophys. J.* 745, 36.
- Fisher, R. and Guhathakurta, M. 1995: *Astrophys. J.* 47, L139.
- Howard, R.A. et al. 2008: *Sp. Sci. Rev.* 136, 67.
- Howard, T.A. and DeForest, C.E. 2012: *Astrophys. J.* 752, 130.
- Hundhausen, A.J. 1972: “Coronal Expansion and Solar Wind”, Springer-Verlag (New York).
- Lyot, B. 1939: *M. Not. Roy. Astron. Soc.* 99, 580.
- Freeland, S.L. and Handy, B.N. 1998: *Sol. Phys.* 182, 497.
- Goelzer, M.L., Schwadron, N.A., & Smith, C.W. 2014: *J. Geophys. Res. Lett.* (in press).
- Howard, R.A. et al. 2008: *Sp. Sci. Rev.* 136, 67.
- Lamb, D.A., DeForest, C.E., Hagenaar, J.J., Parnell, C.E., and Welsch, B.T. 2010: *Astrophys. J.* 720, 1405.
- McComas, D.J., Philips, J.L., Hundhausen, A.J., and Burkepile, J.T. 1991: *Geophys. Res. Lett.* 18, 73.
- McComas, D.J., Gosling, J.T., and Phillips, J.L. 1992: *J. Geophys. Res.* 97, 171.
- McComas, D.J. 1995: *U.S. Nat. Rept. to Intl. Union of Geodesy & Geophysics 1991-1994, Part 1*, p. 603.
- McKenzie, D.E. and Hudson, H.S. 1999: *Astrophys. J.* 519, L93.
- Morrill, J.S. et al. 2008: *Sol. Phys.* 233, 331.
- Neugebauer, M. and Snyder, C.W. 1962: *Science*, 138, 1095.
- Schrijver, C.J., Title, A.M., Hagenaar, H.J., and Shine, R.A. 1997: *Sol. Phys.* 175, 329.
- Schwadron, N.A., Connick, D.E., & Smith, C.W. 2010: *Astrophys. J.* 722, L132.
- Sheeley, N.R., Jr., Lee, D.D.-H., Casto, K.P., Wang, Y.-M., and Rich, N.B. 2009: *Astrophys. J.* 694, 1471.
- Parker, E.N. 1958: *Astrophys. J.* 128, 664.
- Parker, E.N. 1961: *Astrophys. J.* 134, 20.
- Priest, E.R. 1982: “Solar Magnetohydrodynamics”, Kluwer Academic Publishers (Dordrecht)

- Sheeley, N.R. and Wang, Y.-M. 2001: *Astrophys. J.* 562, 107.
- Sheeley, N.R., Knudson, T.N., and Wang, Y.-M. 2001: *Astrophys. J.* 546, 131.
- Sheeley, N.R., Warren, H.P., & Wang, Y.-M. 2004: *Astrophys. J.* 616, 1224.
- Smith, C.W., Schwadron, N.A., & DeForest, C.E. 2013: *Astrophys. J.* 775, 59.
- Verdini, A., Velli, M., & Buchlen, E. 2009: *Astrophys. J.* 700, L39.
- Wang, Y.-M., Sheeley, N.R., Howard, R.A., St. Cyr, O.C., and Simnett, G.M. 1999: *Geophys. Res. Lett.* 26, 1203.
- Zhao, X.P. and Hoeksema, J.T. 2010: *Sol. Phys.* 266, 379.

7. APPENDIX: MOTION FILTERING AND SPEED SPECTRUM ANALYSIS

In this Appendix we describe some of our processing techniques, which may be unfamiliar to the casual reader. In Section 7.1, we describe the basis of Fourier motion filtering, how it works, and why we use it. In Section 7.2, we relate the RMS motion filter that we used to characterize inbound speed vs. altitude over the coronal hole, to the motion filtering described in Section 7.1.

Here we consider images as real or complex functions, mapping $\mathbb{R}^2 \rightarrow \mathbb{R}$ or $\mathbb{R}^2 \rightarrow \mathbb{C}$ as appropriate. Actual digital images are better represented on the integers, mapping $\mathbb{Z}^2 \rightarrow \mathbb{C}$, but the arguments hold for both cases.

7.1. Motion filtering with the Fourier transform

The Fourier transform has many useful properties for image transformation (Bracewell 1999); here we use it for the property of localizing moving features. In particular, a 2-dimensional Fourier transform in the (r, t) plane localizes all features that are moving with speed v to a line of slope $-v$. Thus, the three-step operation of (i) Fourier transforming an (r, t) image to its conjugate (k_r, ω) plane; (ii) filtering the resulting image to keep only pixels with a certain range of the ratio ωk_r^{-1} ; and (iii) inverse Fourier transforming back to the (r, t) plane has the effect of retaining only features moving within the corresponding range of speeds $v = -\omega k_r^{-1}$. The process removes all other features from the final (r, t) image.

Here we demonstrate for the careful but unfamiliar reader that features moving at a given velocity are indeed localized by the Fourier transform, so that they can be retained or removed by masking the Fourier plane. Consider a time-distance image $I(r, t)$ that maps the value of some quantity as a function of position (r) and time (t). Take, as an *ansatz*, that any $I(r, t)$ can be decomposed by velocity:

$$I(r, t) = \int f_v(s_v) dv \quad (2)$$

where each f_v is a separate function of a single variable s_v , with:

$$s_v \equiv r - vt. \quad (3)$$

One obvious example of an $f_v(s_v)$ is an infinite plane wave propagating at speed v , but there is no reason to consider only plane waves. For the following analysis literally any physically relevant function $f(s)$ will suffice. The definition of s_v ensures that the corresponding $f_v(r, t)$ propagates the pattern at the correct speed.

Clearly, if the *ansatz* holds, then it is sufficient to demonstrate that the 2-D Fourier transform localizes all signal energy from just one single $f_v(s_v(r, t))$ to a line $\omega = -vk_r$: since the Fourier transform is a linear operator, the integral in Equation 2 migrates through the transform operator.

The 2-D Fourier transform of $f_v(s_v)$ is just:

$$F_v(k_r, \omega) \equiv \iint e^{-ik_r r} e^{-i\omega t} f_v(r - vt) dr dt, \quad (4)$$

Switching variables to s in favor of r yields:

$$F_v(k_r, \omega) = \iint e^{-ik_r(s+vt)} e^{-i\omega t} f_v(s) ds dt, \quad (5)$$

which is easily separable because f_v depends only on s in this formulation. Evaluating the t integral:

$$F_v(k_r, \omega) = (2\pi)^{-1/2} \delta(vk_r + \omega) \int e^{-ik_r s} f_v(s) ds \quad (6)$$

where δ is the Dirac delta. Clearly, $F_v(k_r, \omega)$ is zero everywhere except where $\omega = -k_r v$, i.e. the line of slope $-v$ in the (k_r, ω) plane. We have demonstrated that the moving pattern $f_v(s_v(r, t))$ is

localized to a particular line by the Fourier transform, without any regard for the actual structure of the function $f_v(s)$.

Furthermore, because of the well-known invertibility of the Fourier transform, and the linearity of both the Fourier transform and its inverse, it is easy to see that the *ansatz* must be true. Clearly any function $F(k_r, \omega)$ may be written as an integral over v of separately-defined $F_v(k_r, \omega)$'s, since the Dirac delta in Equation 6 serves to isolate the values of a particular $F_v(k_r, \omega)$ from those of every other $F_{v'}(k_r, \omega)$, while v spans the entire additional dimension. Therefore every point (k_r, ω) corresponds to a specified (potentially nonzero) value of some $F_v(k_r, \omega)$. Since any function $f(r, t)$ may be represented as the inverse Fourier transform of some $F_v(k_r, \omega)$, the *ansatz* holds. In fact, the transform in Equation 2 is a variant of the well-known *radon transform*, of which speed spectrum analysis is but one application. The radon transform is explored in some detail in Chapter 8.8 of Bracewell (1999).

In short, every image $I(r, t)$ may be represented as the integral over v of a collection of speed-filtered images, each of which contains only features moving at particular speed v . These components are localized in the Fourier plane, and Fourier transformation can be used to isolate them. Speed filters of these types have many applications. In heliophysics, applications include separation of solar photospheric p-modes with phase speeds well above the local sound speed, from surface features that move under the local sound speed (R. Shine, priv. comm. 1999; Lamb et al. 2010); and isolation of solar wind features from quasi-stationary artifacts (DeForest, Howard & Tappin 2011). Interested readers are directed to Chapter 8 of Bracewell (1999) for a range of fascinating insights.

In addition to the obvious benefit of isolating inbound and outbound features from the data, motion filtering with a narrow range of speeds also reduces photon noise in the resulting processed data. Uncorrelated noise, such as photon shot noise, is distributed evenly throughout Fourier space. Zeroing out pixels in the (k_r, ω) plane to reduce the total nonzero pixel count by a factor of α thus reduces the total photon noise in the final (r, t) image by a factor of $\alpha^{1/2}$.

7.2. Speed spectrum analysis by convolution

To identify a pattern of inbound energy versus radius over the South pole of the Sun, we use convolution of an image patch in the (r, t) plane, with a diagonal line. We convolved the image patch with a diagonal line of specified slope v , and took the RMS value of the resulting image patch as an indication of the total number of features moving at approximately speed v in the patch.

By varying both v and the central radius r_{cen} of the patch, we were able to arrive at a map showing the relative distribution of total integrated feature strength versus v and r . This is the incoherent variant of the well-known radon transform (Bracewell 1999, Chapter 8.8).

This process is a quick and easy way to identify patterns in the speed spectrum of inbound waves. In Section 7.1 we demonstrated that a speed spectrum exists – i.e. that any given (r, t) image can be represented as a collection of images, each of which contains only features moving at a particular velocity v . In our case we did not want to represent the individual features, only to estimate the total inbound image energy moving at a given speed, as a function of that speed.

Here we demonstrate that convolution with a diagonal line is equivalent to applying a speed filter in Fourier space as described in Section 7.1. Recall the famous *Convolution Theorem* (e.g. Section 4.17 of Bracewell 1999) that relates convolution in real space to multiplication in Fourier space, and vice versa:

$$f(r, t) * q(r, t) = \mathcal{F}^{-1} (F(k_r, \omega) \otimes Q(k_r, \omega)) \quad (7)$$

where \mathcal{F} represents the Fourier transform, $F \equiv \mathcal{F}(f)$, $Q \equiv \mathcal{F}(q)$, $*$ is the convolution operator, and \otimes is elementwise multiplication.

Consider the ideal straight-line image:

$$q_v(r, t) = \delta(r - vt). \quad (8)$$

Its Fourier transform $Q_v \equiv \mathcal{F}(q_v)$ is easily calculated:

$$Q_v(k_r, \omega) \equiv \iint e^{-i\omega t} e^{-ik_r r} \delta(r - vt) dr dt, \quad (9)$$

which may be performed by inspection since one of the two integrals is done by the δ and the other itself yields a δ :

$$Q_v(k_r, \omega) = (2\pi)^{-1} \delta(k_r v + \omega), \quad (10)$$

which is a single-speed filter in the Fourier plane. Equation 10 should not be a surprise, since $q_v(r, t)$ matches the form of 3 in Section 7.1.

Hence, convolution with a straight line is equivalent (up to a multiplicative constant) to Fourier filtering with a perpendicular straight line. By neglecting to propagate constant values in convolving our image patches with various straight lines, we lost any photometric quality to the remaining RMS value of the image patch after filtration – but as we were interested in detecting a pattern in the surviving optical flow, rather than in quantifying the total image energy in that flow, simple convolution was sufficient.